Brazilian Journal of Physics (2024) 54:141
https://doi.org/10.1007/s13538-024-01513-y

Autocorrelation Optical Coherence Tomography (Au-OCT) of Complex Morphologies and Moving Samples

Marcus Paulo Raele[1] · Marcello Magri Amaral[2] · Noé Gabriel Pinheiro Machado[1] · Anderson Zanardi de Freitas[1]

Received: 18 March 2024 / Accepted: 4 June 2024 / Published online: 21 June 2024

Abstract
Optical coherence tomography (OCT) systems are renowned for image construction using interferometric signals. While autocorrelation signals are often seen as unwanted artifacts in OCT images, this research diverges by extracting meaningful information from them in order to crate tomographic images. This approach boasts simplicity, cost-effectiveness, and immunity to axial movement during imaging. However, it sacrifices accuracy in reconstructing certain sample characteristics, potentially causing morphological distortions. Nonetheless, valuable structural insights can still be gleaned. Employing Fourier domain-based autocorrelation OCT (Au-OCT) with specific equipment, various samples were scanned under different conditions, including movement. Au-OCT proved resilient to vibrations and minor movements, without the need for an external reference mirror. These results endorse its viability for biological and industrial sample analyses, even in scenarios involving multilayered objects.

Keywords Autocorrelation · Low coherence interferometry · LCI · Cross correlation

1 Introduction

Optical coherence tomography (OCT) [1] is an imaging technique that utilizes interferometry with short-coherence light to achieve micrometer-level depth resolution. It employs transverse scanning of the light beam to form two- and three-dimensional tomographic images of biological tissues or other scattering media. The primary source of image contrast in optical coherence tomography (OCT) is the scattering properties of the media, which are intrinsic to the light-tissue interaction. This enables detailed, label-free visualization of subsurface structures in translucent or opaque materials. In essence, OCT employs a Michelson interferometer and a broadband, near-infrared light source that emits a beam, which is split into two paths by a beamsplitter. One part of the light beam is directed to the reference arm and reflected by a reference mirror back to the beamsplitter. The other part of the light beam is directed towards the sample being imaged. The light is focused and scanned across the desired imaging area, and the backscattered light from the sample recombines with the reference beam at the beamsplitter. Due to the different path lengths traveled by light in each arm (reference vs. scattered from the sample), an interference pattern is created when the beams recombine.

There are two main types of OCT systems [2] differentiated by their approach to analyzing the light source and resulting interference pattern: time-domain OCT (TD-OCT) and Fourier-domain OCT (FD-OCT). The first OCT design was TD-OCT, which employs a single detector and obtains depth information by physically moving the reference arm back and forth, changing its optical path length. Despite its relatively simple design, TD-OCT has lower depth resolution due to limitations in precisely controlling the reference arm movement. It is more susceptible to motion artifacts because of the physical movement of the reference arm and has slower scan speeds compared to FD-OCT methods.

FD-OCT, on the other hand, detects and analyzes the spectral interference pattern. The entire spectrum of the resulting interference pattern is captured by a spectrometer simultaneously, and by applying a Fourier transform analysis to the recorded signal, the depth information of the imaged sample is obtained. This modality is faster compared to TD-OCT, reducing motion artifacts. FD-OCT is further divided

✉ Marcus Paulo Raele
mpraele@ipen.br

[1] Nuclear and Energy Research Institute, IPEN, CNEN/SP, Av. Prof. Lineu Prestes, São Paulo, SP 2242CEP05508-000, Brazil

[2] Biomedical Engineering, Universidade Brasil, Rua Carolina Fonseca 235, São Paulo, SP, CEP 08230-030, Brazil

into two implementations: spectral domain OCT (SD-OCT) and swept-source OCT (SS-OCT). They differ in hardware implementation; SD-OCT uses a broadband light source and a spectrometer, while SS-OCT employs a tunable laser source that rapidly sweeps across a range of wavelengths, allowing for even faster acquisition speeds compared to standard SD-OCT.

The image use of OCT as described provides structural information about the sample and its optical properties. On the other-hand, functional OCT (fOCT), a modification on the acquisition and data analysis, captures information about tissue function by measuring parameters sensitive to physiological processes, such blood flow (OCT angiography), [3] oximetry (visible light OCT), [4] and metabolic activities (dynamic contrast OCT) [5]. The ability to use OCT to measure depth resolved structural, functional, and optical features is attractive to several area of application. This technology has become essential clinical technique in ophthalmology for diseases diagnoses, such of age-related macular degeneration (AMD) [6, 7] and diabetic retinopathies [8]. OCT also finds application in other medical fields such cardiology, [9, 10] dermatology, [11, 12] gastroenterology, [13] and neurology, [14] and in non-medical fields such as agriculture [15] and industry [16]. Despite a valuable optical imaging tool, OCT presents some limitations. Two of the OCT limitations are the image depth and motion artifacts. The image depth is limited by the light penetration, which is affected by the light-tissue interaction, highly scattering media like blood or bone can significantly attenuate the light signal. Sample movement can introduce image artifacts and make it difficult to interpret the image and perform measurements. Moreover, if the motion in the axial direction is larger than the image range, no signal from the sample can be obtained.

As stated before, OCT signal is a function of the optical path length difference between the reference and sample arms. If the reference can be changed in synchrony with sample axial motion one could always obtain the OCT signal. One way to obtain such of synchrony is by replacing the reference mirror by the high reflectance surface of the sample, creating the so-called self-interference or autocorrelation OCT (Au-OCT) image. In this work, we overview theoretical basis of OCT identify how to obtain the Au-OCT; we describe and implement the Au-OCT optical setup and tested our approach to obtain the depth information of scattering samples under highly vibration environmental conditions.

2 OCT Fundamentals

To understand how the here proposed Au-OCT method obtains the depth information of scattering samples under highly vibration environmental conditions, we first briefly revise the fundamentals of OCT interferometry. OCT uses a Michelson interferometer, as depicted in Fig. 1, using a reference mirror to precisely determine the optical delay and determine the spatial location of individual structures within the sample. By developing the low coherence interferometry equations (complete demonstration can be found on literature [17–19]). The light source spectrum $S(k)$ is divided into the reference and sample arms by the beamsplitter. The reference mirror reflects the light with a reflectance a_r at the r position. Similarly, the sample backscatters the light with a power $a_s(z)$, as a function of the axial position z. After recombining in the beam splitter, the resulting spectral interference intensity $I(k)$, Eq. 1, contains the sample structural depth profile information.

$$I(k) = S(k)\left|a_r e^{i2kr} + \int_0^\infty a_s(z) e^{i2k(r+z)} dz\right|^2 \tag{1}$$

For simplicity, assuming a perfect mirror at the reference arm $a_r(r)=1$, and setting $r=0$, Eq. 1 reduces to Eq. 2. Setting $r=0$ is possible because in an interferometric setup only the difference between the optical path lengths between reference and sample arms matters, so we can arbitrarily set r to zero.

$$I(k) = S(k)\left|1 + \int_0^\infty a_s(z) e^{i2kz} dz\right|^2 \tag{2}$$

Expanding the square modulus, applying the Fourier identity, and considering the symmetric Fourier properties, let us assume $\hat{a}_s(z) = a_s(z) + a_s(-z)$, one can find Eq. 3. One can find the stepwise description under the reference [19].

$$I(k) = S(k)\left(1 + 2\int_{-\infty}^{\infty} \hat{a}_s(z) e^{-i2knz} dz + \iint_{-\infty}^{\infty} \hat{a}_s(z)\hat{a}_s(z\prime) e^{-i2kn(z-z\prime)} dz dz\prime\right) \tag{3}$$

The third term of the sum inside the parentheses is the autocorrelation (AC) term. We can also rewrite the two integrals as the Fourier transform of $\hat{a}_s(z)$ and the $AC[\hat{a}_s(z)]$, Eq. (4). Finally, to recovery the depth backscattering profile $\hat{a}_s(z)$, an inverse Fourier transformation can be applied over Eq. 4, resulting in Eq. 5.

$$I(k) = S(k)\left(1 + \frac{1}{2}\mathcal{F}\{\hat{a}_s(z)\} + \frac{1}{8}\mathcal{F}\{AC[\hat{a}_s(z)]\}\right) \tag{4}$$

$$\mathcal{F}^{-1}\{I(k)\} = \mathcal{F}^{-1}\{S(k)\} \otimes \left([\delta(z)] + \frac{1}{2}\hat{a}_s(z) + \frac{1}{8}AC[\hat{a}_s(z)]\right) \tag{5}$$

$$= A \otimes (B + C + D) \tag{6}$$

where $A = \mathcal{F}^{-1}\{S(k)\}$, $B = [\delta(z)]$, $C = \frac{1}{2}\hat{a}_s(z)$, and $D = \frac{1}{8}AC[\hat{a}_s(z)]$.

Analyzing each term separately, 'A' contains information about the light source coherence length (axial resolution). '$A \otimes B$' is a dc signal representing the convolution of

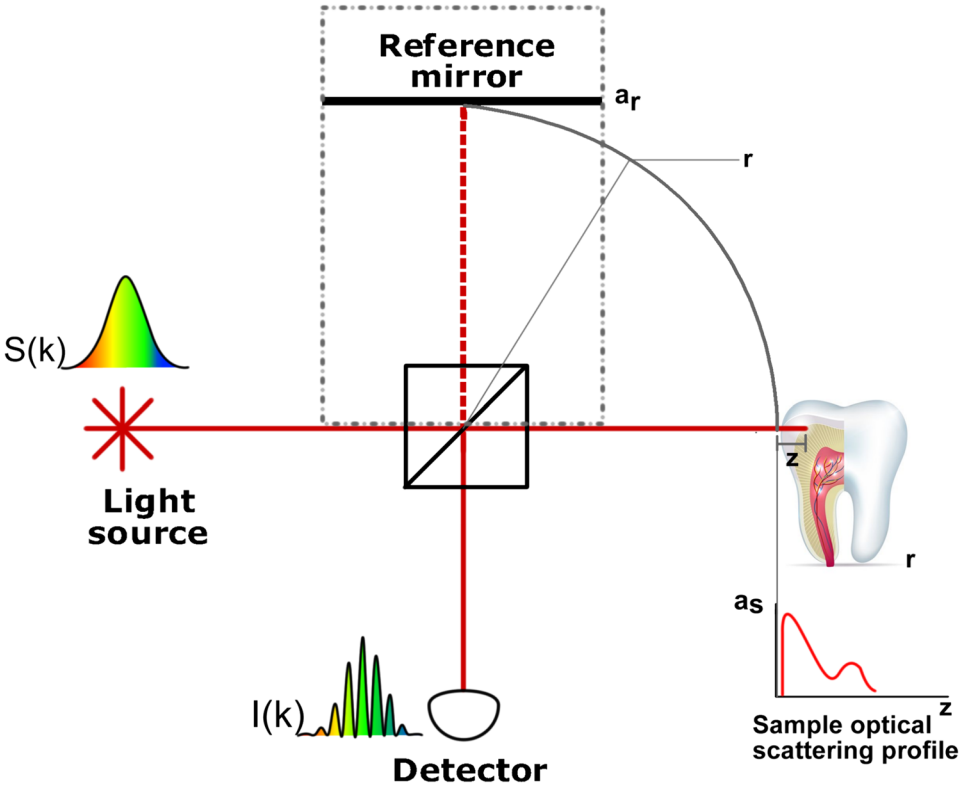

Fig. 1 OCT optical setup, based in a Michelson interferometer. Light from the source is divided and directed towards both the reference mirror and the sample, where it is reflected by the sample's surface and inner structures. The reflected light from these features recombines and is captured by the photodetector. In an Au-OCT setup, the reference arm is not necessary. Instead, the system analyzes only the light reflected from different depths within the sample, specifically the interference between them

the light source coherence length with the reference mirror scattering profile (delta-like function). '$A \otimes C$' is the cross-correlation term, corresponding to the conventional OCT signal. This term involves the convolution of the reference mirror scattering profile with the sample scattering profile. '$A \otimes D$' is the autocorrelation signal term, representing the mutual interference between all the layers within the sample.

3 Autocorrelation OCT (Au-OCT)

By removing the reference mirror from the OCT setup (Fig. 1 without the dash-dot region), the Eq. 6 reduces to the autocorrelation term ('$A \otimes D$'). In principle, the absence of a reference should turn the autocorrelation signal challenging interpret. The autocorrelation signal only provides information about distances between any two reflective structures within the sample. Figure 2 illustrates the morphological bias present in the autocorrelation interferometry imaging (Au-OCT). In the figure, the letters i, j, and k identify the structures, and the pairs of them indicate the mutual interference responsible for the reconstruction of specific structures.

However, in a real scenario, things can unfold quite differently. It is often the case that samples exhibit high reflectivity at the first surface, due to a high refractive index mismatch between the surround media and the sample. Under this condition, the reflectance of the first surface of sample acts as the 'reference mirror.' The OCT signal is formed mainly by the interference between the

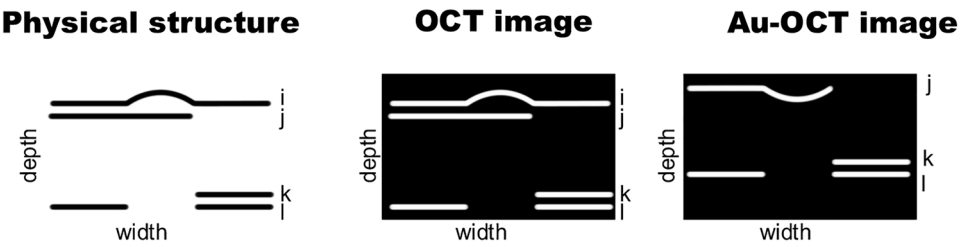

Fig. 2 At the first column, a schematic illustration of a hypothetical sample, where the black horizontal lines represents scattering surfaces. The OCT images, at the second column, map the physical structure correctly. In the other hand, at the third column, the Au-OCT image could misinterpret the sample, leading to images with no correspondence with reality. The dotted line represents the surface of reference (missed information)

reflectance of the first surface and the internal scattering of the sample. In other words, referring to the definitions in Fig. 2, the signal of '*i*' and all other structures would contribute differently than those without '*i*,' making other contributions negligible. From this perspective, one might perceive this approach as cross-correlation interferometry term present in Eq. 5. However, despite the reflectance from the first surface being stronger than the scattering from the inside structures of the sample, it is not a delta function such in the case of a mirror use. It is essential to recognize that the entire backscattered signal, encompassing all mutual interferences, is captured by the system, making it a genuine autocorrelation system. By removing the reference mirror, one replaces an external zero delay (or reference) by the sample first surface zero delay. In this way, all the images obtained by this configuration should be flatten. Despite the loss of topographic information, Au-OCT can offer advantages in some situations. For instance, the Au-OCT system's insensitivity to vibration and movement along the axial direction, there is no need for image registration, which is a computational and time-consuming process. In many OCT applications, the sample optical attenuation coefficient is measured for differential diagnosis. It requires the use of image registration and flattening algorithms before the OAC measurement. In other cases, one might be interested in measuring the thickness of internal structures or layer integrate, e.g., both scenarios could benefit from this method. Samples like teeth or nails exhibit a stronger reflection due to the higher refractive index ($n \sim 1, 6$) [20] and their surface smoothness of these provides higher specular like reflection, making it more suitable to Au-OCT.

It is important to note that this approach is not intended to replace OCT systems but rather to complement the capabilities within the realm of optical coherence tomography. For some class of samples be like soft tissues, which presents lower intensity light reflection due to the smaller refractive index ($n \sim 1, 4$) [21], or applications where the sample topography is a important feature, conventional OCT could still the best choice.

In the literature, only a limited number of studies have addressed the use of the autocorrelation signal in OCT. Most of these studies focus on autocorrelation as a potentially detrimental signal in OCT images and aim to eliminate it, as demonstrated by Wang et al. [22], Vergnole et al. [23], and Moon et al. [24]. Similarly, Shalaby et al. [25] and Nandakumar et al. [26] have pursued the same objective.

A few studies have discussed the possibility of using the autocorrelation signal to extract useful information. For instance, Lychagov et al. [27] demonstrated its application in measuring the distances between glass slides. Similarly, Fercher et al. [28] utilized the autocorrelation signal to measure intraocular distances, although no imaging was performed in their study. Additionally, Modell et al. [29] presented a setup capable of selecting specific autocorrelation signals from a sample.

In this way, although many studies have exploited the Au signal to extract useful data from samples, none of them have performed comprehensive images from complex structured samples. The Au-OCT have some advantages over OCT in specific cases, such as axial movement insensitiveness, leading to the objective and originality of the present work: perform and compare images from autocorrelation signal with regular OCT.

4 Au-OCT Setup Implementation

This study was performed using a pigtailed super luminescent light-emitting diode SLED (Qphotonics Inc., Virginia, model QSDM-830–2) with emission centered at 831 nm, spectral bandwidth of 26 nm, and optical power of 2 mW @ 195 mA, providing an axial resolution of 11.7(5) µm. The SLED output was coupled in an optical circulator (Thorlabs Inc., New Jersey, model PIOC850000THL01). The light was guided through the optical circulator to the collimator (Thorlabs Inc., New Jersey, F240APC-C), then, a scanner system (GSI LUMONICS Inc., California, USA) and a scan lens (Thorlabs Inc., New Jersey, model LSM03-B3).

The reflected light by the sample was collected through the same optical path to the optical circulator, which led the backscattered light to the spectrometer (model USB4000, spectral range 599–898 nm, Ocean Optics Inc, Dunedin, Florida, USA). Figure 3 illustrates the setup. The signal processing followed the methodology described by Dorrer et al. [30].

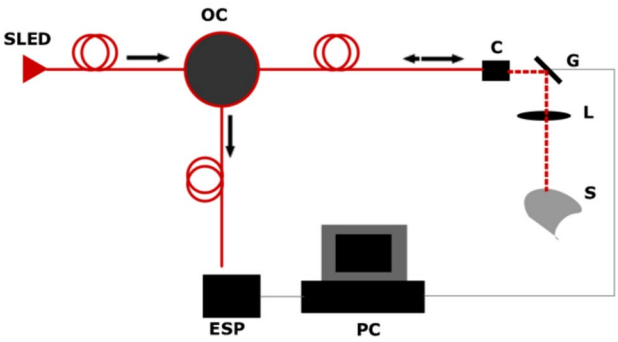

Fig. 3 The optical setup: The super luminescent LED (SLED) was coupled to the optical circulator (OC) which was coupled to the collimator (c). The light beam was then guided by the optical fiber till the galvanic scanner system (G) and focused by the scanning lens (L) at the sample (S). The back scattered light performed the inverse route and guided to the spectrometer (ESP), where the interferometric pattern was analyzed

5 Validation

For validation, a commercial OCT (model spectral radar 930 nm with 6.2 µm of axial resolution, Thorlabs Inc, Norfolk, Virginia, USA) was used to compare results with the setup under study in this work.

6 Results and Discussion

Measuring a Scotch tape roll as a dummy sample was done in order to test the setup. The regular OCT image is presented as the gold standard in Fig. 4. In the Au-OCT image, it is possible to detect the tape layers even at deeper levels. Both images exhibit the same morphological features, accounting for differences between techniques. In both images light scattering centers formed by air gaps smaller than the system resolution are visible.

By imaging a double-sided tape, a more diffuse reflective sample (first column of Fig. 5), the striping peel (waxed paper), had a very smooth surface, making it easier, due to its more specular-like reflection, to perform Au-OCT. More than one layer of different materials could be visualized, and the image morphology matched that of the OCT images.

The image of a prosthetic tooth, Fig. 5 middle column, interestingly shows two distinct layers, suggesting that the prosthetic tooth was produced in two steps first the core and later the shell. Microbubble-like structures also were found in the image and was identified as quartz or glass beads, commonly used to improve sample's physical strength.[31] The Au-OCT was again capable of detecting the same information, albeit with a bit more noise in the images. Finally, a human tooth was used; recorded images are shown at Fig. 5 last column. Two layers were easily identified, as expected the enamel and dentin underneath are visible in both techniques.

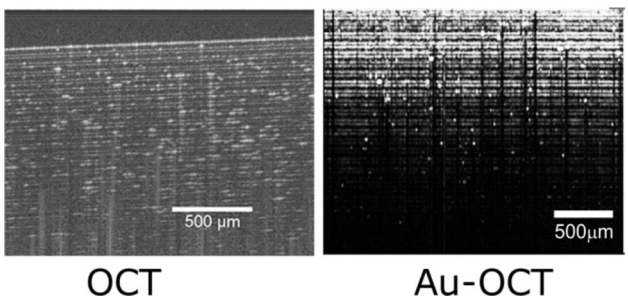

Fig. 4 OCT and Au-OCT images of scotch tape roll at left and at middle, respectively. At the right, the integrated scattering profile of the Au-OCT image. The solid line represents the data and the dashed fitting, showing the oscillation in the scattering intensity

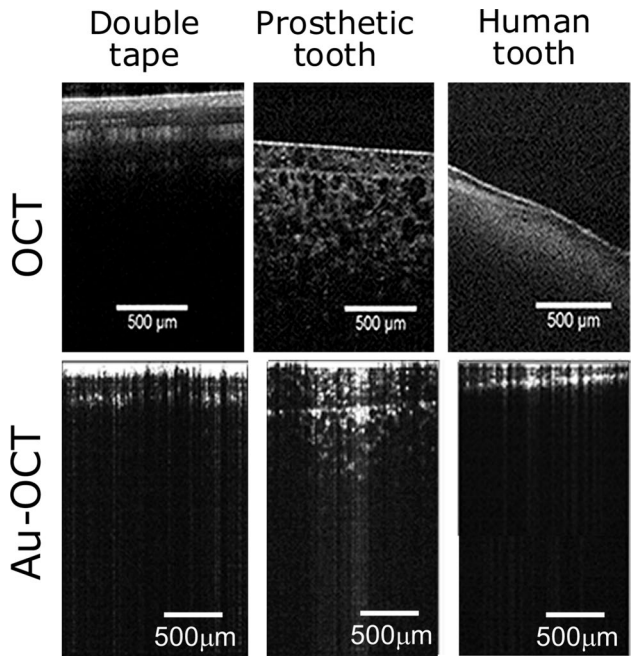

Fig. 5 OCT images at the top and Au-OCT at the bottom for the following samples, respectively: double sided tape, prosthetic tooth, and human tooth

Despite different, Au-OCT images present the same features observed in the conventional OCT images. The advantage of Au-OCT over OCT becomes clear when the sample starts to move in the axial direction.

6.1 Moving Sample Test

To demonstrate that the Au-OCT is non-sensitive to movements in the axial direction, we attached histological slide, 175(5) µm thick, to a loudspeaker connected to a function generator (model F62A; Wavetek San Diego, Inc., San Diego, USA), configured to produce a sinusoidal pattern with frequencies ranging from 0 to 1000 Hz. Images were once again captured with an the Au-OCT and OCT to compare the results, as shown in, Fig. 6.

Setting the function generator to 0 Hz, steady images were obtained with both systems for comparison and to detect any possible abnormalities. The images can be seen in Fig. 6, confirming that both systems were working as expected. At 15 Hz, when using the OCT system, a wave pattern is observed due to the combination of B-scan speed and the movement of the speaker, while with Au-OCT, the image remained steady. At 100 Hz, the phenomenon was even more pronounced, yet the Au-OCT continued to behave as if there was no movement at all. The focal geometry (confocal parameter) did not cause perceptible changes in intensity for Au-OCT with this displacement size.

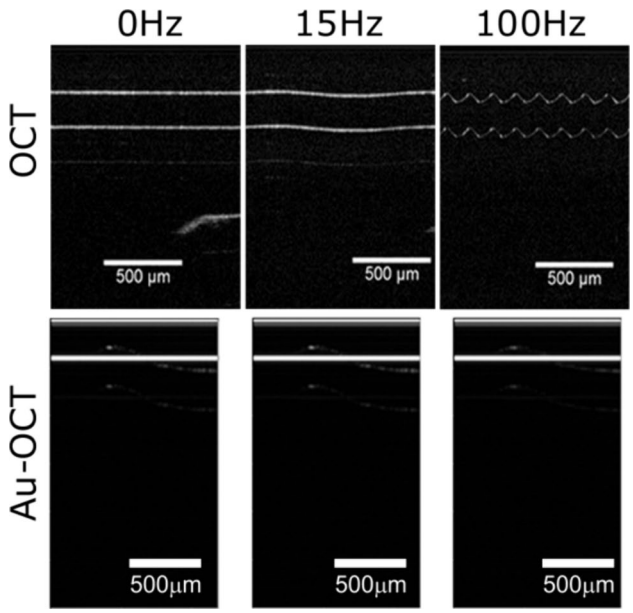

Fig. 6 OCT and Au-OCT images of a glass slide from rest till 100 Hz of oscillating motion. Is it possible to verify that Au-OCT images remain the same independently of neither the frequency nor the amplitude

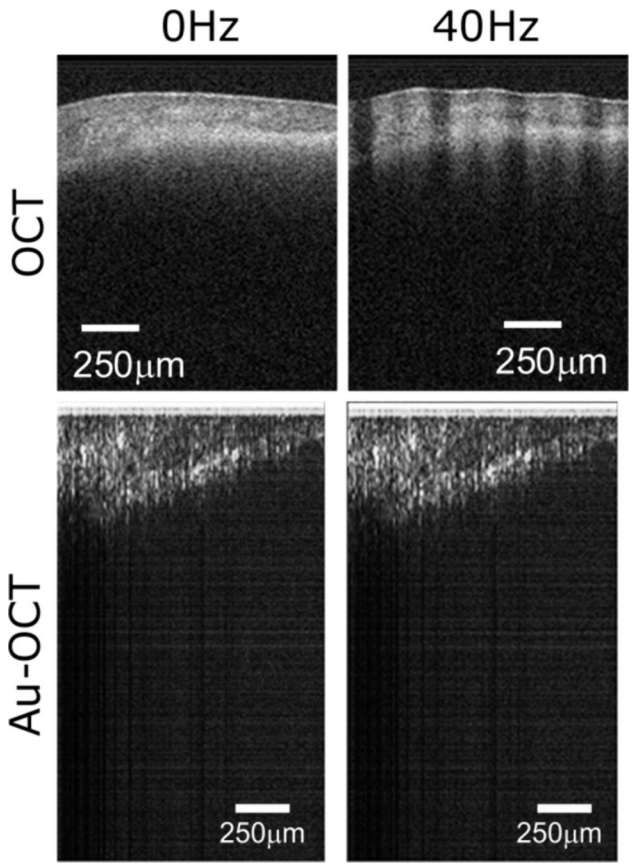

Fig. 7 Human tooth imaged by OCT (upper row) and Au-OCT (bottom row), at rest (left) and moving (right). The OCT image becomes distorted when the sample starts to vibrate

Images of a human tooth were captured with the sample both still and vibrating at 40 Hz, as shown in Fig. 7. The Au-OCT performed images with no deformations or problems due to the sample movement, showing its vocation to perform images in live/moving situations and in environments where vibration cannot be avoided, as found in industries or living subjects imaging.

One of the benefits of using Au-OCT to image moving samples is that averaging multiple B-scan becomes a straightforward process. Averaging multiple B-scan is a powerful and broadly used method to reduce a variety of noises[32] including speckle [33] in OCT. Comparing the average of five B-scans acquired at the same location for a static and moving dummies sample (Fig. 8), it is possible to verify that, in situations without movement (Fig. 8 left column), both systems can observe the same sample properties, reconstructing the sample's physical morphology correctly. However, when the sample starts to move (Fig. 8 middle column), conventional OCT loses crucial morphological information showing a wavy tomographic profile of tape layers, even mixing layers causing false structures due to the beating between sample movement. The average image obtained from conventional OCT image became blurred when the image is acquired under vibration (Fig. 8 top right), while the same results is obtained using the Au-OCT (Fig. 8 bottom right). Additionally, the Au-OCT presented a clear image with reduced noise (boxes "a" and "b" at Fig. 8) due to the proper averaging process, showing the practical advantages of the proposed approach.

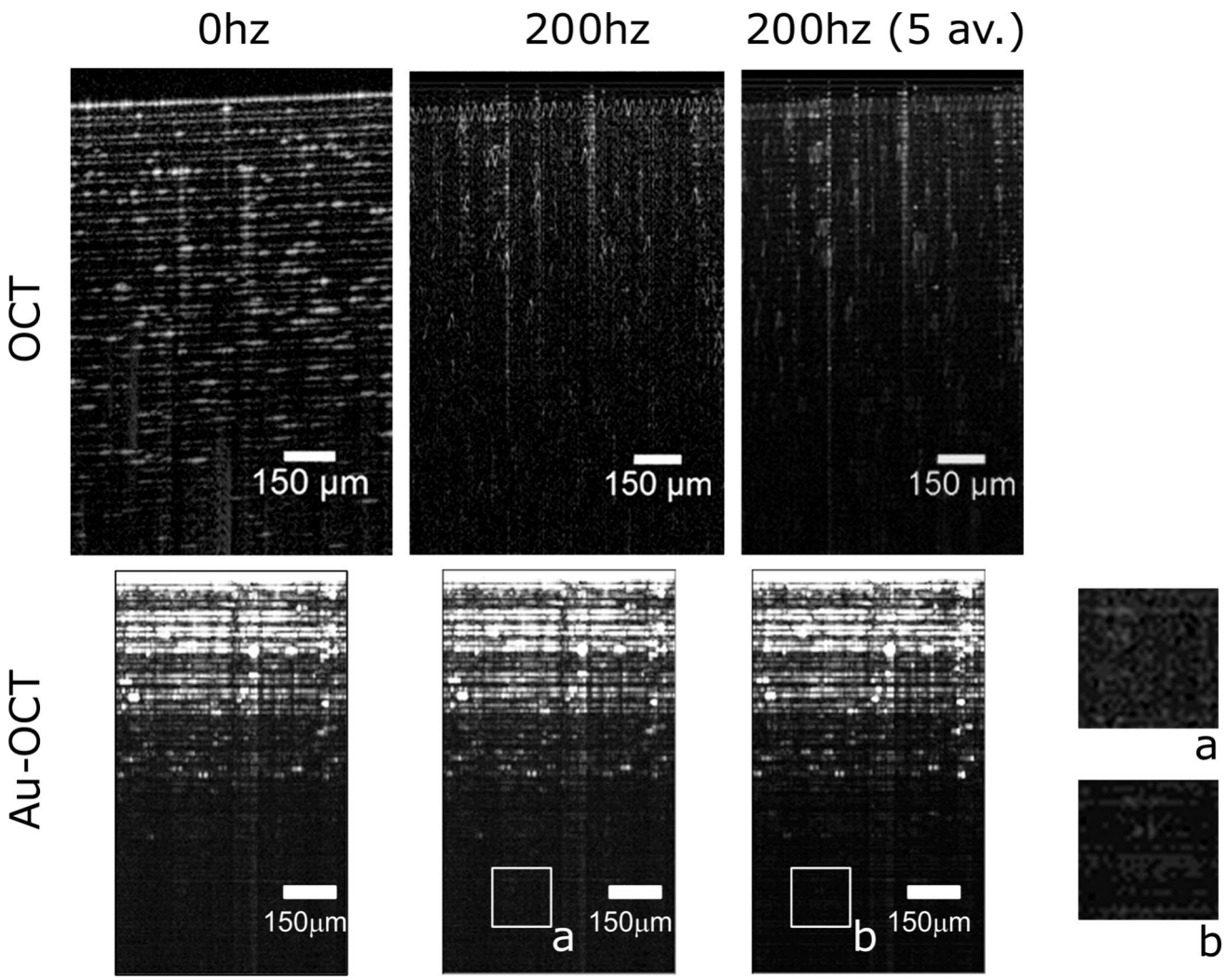

Fig. 8 Images of a scotch tape roll, at the first row OCT and at second row Au-OCT. The first column shows the samples at rest, second column samples in motion @200 Hz, again the OCT exhibits morphological distortion while Au-OCT does not. At the last column sample moves @200 Hz and an averaging of 5 a-scans were performed. The OCT image is completely blurred, and the Au-OCT shows better quality than sample at rest due to the averaging

7 Conclusions

The use of conventional OCT to image samples under fast axial motion prevents the technique to obtain reliable and useful information regarding the sample optical properties. The herein proposed Au-OCT solve this problem by replacing the reference mirror of the OCT interferometer by the reflection of the air-sample interface. We demonstrated the use of Au-OCT to image a variety of samples, as long as the first surface reflection has sufficient reflectivity. For industrial applications in plastic films and multi layered transparent media imaging, where there is simple, layered, and glossy structured, the Au-OCT could provide reliable dimensional measurements under highly vibration environmental. For biological application, the technique also shown potential for measuring a class of problems where the important feature is how the light propagates inside the sample, such for measuring the optical attenuation coefficient differences between sound and abnormal tissue. For example, is to obtain this feature from tooth structures, such as enamel. One limitation of the Au-OCT is that it relies on the first surface reflectance of the sample, typically the air-sample interface. The maximum reflectance is achieved when the objective lens focus is positioned at this interface. If the samples away from the focus, the reflectance can be reduced, reducing the image contrast. Even though, interferometric technique has a high sensitivity, so it can still produce useful images for several applications. Finally, future application on odontology and dermatology for differential diagnosis, as well as industrial application for non-destructive evaluation in real-time manufacturing process, can benefit from this technology and will be explored in future work.

Acknowledgements We thank FAPESP (2009/13764-3, 2017/21851-0 and 2015/24878-0) and PRPG-USP for helping this study with financial support. Authors thank the Brazilian National Council for Scientific and Technological Development – CNPq, grants INFO 465763/2014-6 and Sisfóton 440228/2021-2.

Author Contributions Dr. Raele conceived the experiment, oversaw its execution, and analyzed the results, while Ms. Machado implemented the setup and contributed to the writing process. Dr. Freitas contributed to the study by conducting data analysis and assisting in the writing process. Amaral contributed revising the data analysis, text and also discussing the results.

Funding We thank FAPESP (2009/13764–3, 2017/21851–0, and 2015/24878–0) and PRPG-USP for helping this study with financial support. The authors thank the Brazilian National Council for Scientific and Technological Development–CNPq, grants INFO 465763/2014–6 and Sisfóton 440228/2021–2.

Data Availability No datasets were generated or analysed during the current study.

Declarations

Competing Interest The authors declare no competing interests.

References

1. D. Huang et al., Optical coherence tomography. Science **254**(5035), 1178–1181 (1991) ISSN 0036–8075.
2. B.E. Bouma et al., Optical coherence tomography. Nat. Rev. Methods Primers **2**(1), (2022).
3. C. L. Chen, Wang, R. K. Optical coherence tomography based angiography Invited. Biomed. Opt. Express. **8**(2), 1056–1082 (2017). ISSN 2156–7085.
4. J. Yi, et al. Visible-light optical coherence tomography for retinal oximetry. Opt. Lett. **38**(11), 1796–1798 (2013). ISSN 0146–9592.
5. C. Ren, et al. Dynamic contrast optical coherence tomography (DyC-OCT) for label-free live cell imaging. Commun. Biol. **7**(1), (2024).
6. Y. Wang, et al. Machine learning based detection of age-related macular degeneration (AMD) and diabetic macular edema (DME) from optical coherence tomography (OCT) images. Biomed. Opt. Express. **7**(12), 4928–4940 (2016). ISSN 2156–7085.
7. J.N. Leuschen, Spectral-domain optical coherence tomography characteristics of intermediate age-related macular degeneration. Ophthalmology **120**(1), 140–150 (2013). ISSN 0161–6420.
8. P.L Nesper, et al. OCT angiography and visible-light OCT in diabetic retinopathy. Vis. Res. **139**, 191–203 (2017). ISSN 0042–6989.
9. D. A. Jones, et al. Angiography alone versus angiography plus optical coherence tomography to guide percutaneous coronary intervention outcomes from the Pan-London PCI cohort. Jacc-Cardiovasc. Interv. **11**(14), 1313–1321 (2018). ISSN 1936–8798.
10. M. M. Viscusi, et al. Current applications and new perspectives in optical coherence tomography (OCT) coronary atherosclerotic plaque assessment: from PCI optimization to pharmacological treatment guidance. Photonics. **10**(2) (2023).
11. N. M. Israelsen, et al. The value of ultrahigh resolution OCT in dermatology - delineating the dermo-epidermal junction, capillaries in the dermal papillae and vellus hairs. Biomed. Opt. Express. **9**(5), 2225–2250 (2018). ISSN 2156–7085.
12. L. M. C. Vasquez-Pinto, et al. Optical coherence tomography applied to tests of skin care products in humans - a case study. Skin Res Technol. **21**(1), 90–93 (2015). ISSN 0909–752X;1600–0846.
13. H. B. Luo, et al. Human colorectal cancer tissue assessment using optical coherence tomography catheter and deep learning. J. Biophotonics. **15**(6), (2022). ISSN 1864–063X.
14. A. Wylegala, Principles of OCTA and applications in clinical neurology. Curr. Neurol. Neurosci. Rep. **18**(12) (2018). ISSN 1528–4042.
15. S.A. Saleah, et al. Optical coherence tomography as a non-invasive tool for plant material characterization in agriculture: a review. Sensors. **24**(1) (2024).
16. X. Lu, et al. Visualization of CO_2 electrolysis using optical coherence tomography. Nat. Chem. (2024).
17. B. E. Bouma, G. J. Tearney, Handbook of Optical Coherence Tomography. In: (Ed.). New York: Marcel Dekker, 2002. cap. 12-Spectral Radar: OCT in the Fourier Domain, p.x, 741 p. ISBN 0824705580 (alk. paper).
18. P. Andretzky, M. Knauer, F. Kiesewetter, G. Haeusler. Optical coherence tomography by spectral radar: improvement of signal-to-noise ratio. Coherence Domain Optical Methods in Biomedical Science and Clinical Applications IV. VALERY, V. T. A. J. A. I. A. J. G. F.: SPIE. 3915**:** 55 -- 59 p. 2000.
19. MA. Bail, G. Haeusler, JM. Herrmann, F.Kiesewetter, MW.Lindner, A. Schultz. Optical coherence tomography by spectral radar for the analysis of human skin. Optical and Imaging Techniques for Biomonitoring III. HANS-JOCHEN FOTH AND RENATO MARCHESINI AND HALINA PODBIELSKA, M. D. A. A. K.: SPIE. 3196**:** 38 -- 49 p. 1998.
20. C. Mujat, et al. Optical path-length spectroscopy of incipient caries lesions in relation to quantitative light-induced fluorescence and lesion characteristics. Appl. Opt. **42**(16), 2979–2986 (2003). ISSN 1559–128X.
21. Y. Zhou, et al. Characterizing refractive index and thickness of biological tissues using combined multiphoton microscopy and optical coherence tomography. Biomed. Opt. Express. **4**(1), 38–50(2013). ISSN 2156–7085.
22. R. K. Wang, Z. A. Ma, practical approach to eliminate autocorrelation artefacts for volume-rate spectral domain optical coherence tomography. Phys. Med. Biol. **51**(12), 3231–3239 (2006). ISSN 0031–9155.
23. S. Vergnole, et al. Common Path swept-source OCT interferometer with artifact removal - art. no. 68472W. Conference on Coherence Domain Optical Methods and Optical Coherence Tomography in Biomedicine XII. San Jose, CA. (2008). W8472-W8472 p.
24. S. B. Moon, Y. Q. Qu, Z.P. Chen, Characterization of spectral-domain OCT with autocorrelation interference response for axial resolution performance. Opt. Express. **26**(6), 7253–7269(2018). ISSN 1094–4087.
25. M. Shalaby, S.S. Al-Sowayan, Autocorrelation noise free optical coherence tomography using the novel concept of resonant OCT (ROCT). J. Eur. Opt. Soc. Rapid Publ. **12** (2016). ISSN 1990–2573.
26. H. Nandakumar, S.P. Mallick, S. Srivastava, Complete removal of arbitrarily strong and arbitrarily located auto correlation artifacts in spectral domain optical coherence tomography: demonstration of an efficient and cost effective technique. Preprints, 2020.
27. V. V. Lychagov, et al. Method for remote diagnostics of the internal structure of layered media. Quantum Electron. **38**(6), 563–569 (2008). ISSN 1063–7818.
28. A. F. fercher, et al. Measurement of intraocular distances by backscattering spectral interferometry. Opt. Commun. **117**(1–2), 43–48 (1995). ISSN 0030–4018.
29. M. D. Modell, et al. Autocorrelation low coherence interferometry. Opt. Commun. **281**(8), 1991–1996 (2008). ISSN 0030–4018.
30. C. Dorrer, et al. Spectral resolution and sampling issues in Fourier-transform spectral interferometry. J Opt. Soc. Am. B: Opti Phys. **17**(10), 1795–1802 (2000) . ISSN 0740–3224.

31. I. Ahmad, Protocols for Predictable Aesthetic Dental Restorations. Wiley (2008). ISBN 9781405173216.
32. R. Leitgeb, C.K. Hitzenberger, A.F. Fercher, Performance of fourier domain vs. time domain optical coherence tomography. Opt. Express **11**(8), 889–894(2003). ISSN 1094–4087.
33. S. G. Proskurin, Raster scanning and averaging for reducing the influence of speckles in optical coherence tomography. Quantum Electron. **42**(6), 495–499 (2012). ISSN 1063–7818.